Biomedical Optics EXPRESS

In vivo imaging of functional microvasculature within tissue beds of oral and nasal cavities by swept-source optical coherence tomography with a forward/side-viewing probe

Woo June Choi and Ruikang K. Wang*

Department of Bioengineering, University of Washington, 3720 15th NE, Seattle, WA 98195, USA
*wangrk@uw.edu

Abstract: We report three-dimensional (3D) imaging of microcirculation within human cavity tissues *in vivo* using a high-speed swept-source optical coherence tomography (SS-OCT) at 1300 nm with a modified probe interface. Volumetric structural OCT images of the inner tissues of oral and nasal cavities are acquired with a field of view of 2 mm × 2 mm. Two types of disposable and detachable probe attachments are devised and applied to the port of the imaging probe of OCT system, enabling forward and side imaging scans for selective and easy access to specific cavity tissue sites. Blood perfusion is mapped with OCT-based microangiography from 3D structural OCT images, in which a novel vessel extraction algorithm is used to decouple dynamic light scattering signals, due to moving blood cells, from the background scattering signals due to static tissue elements. Characteristic tissue anatomy and microvessel architectures of various cavity tissue regions of a healthy human volunteer are identified with the 3D OCT images and the corresponding 3D vascular perfusion maps at a level approaching capillary resolution. The initial finding suggests that the proposed method may be engineered into a promising tool for evaluating and monitoring tissue microcirculation and its alteration within a wide-range of cavity tissues in the patients with various pathological conditions.

OCIS codes: (170.4500) Optical coherence tomography; (170.2655) Functional monitoring and imaging; (170.1470) Blood or tissue constituent monitoring.

References and links

1. American Cancer Society. Cancer Facts & Figs. 2014.
2. M.-T. Tsai, H.-C. Lee, C.-K. Lee, C.-H. Yu, H.-M. Chen, C.-P. Chiang, C.-C. Chang, Y.-M. Wang, and C. C. Yang, "Effective indicators for diagnosis of oral cancer using optical coherence tomography," Opt. Express **16**(20), 15847–15862 (2008).
3. R. Byakodi, S. Byakodi, S. Hiremath, J. Byakodi, S. Adaki, K. Marathe, and P. Mahind, "Oral cancer in India: an epidemiologic and clinical review," J. Community Health **37**(2), 316–319 (2012).
4. M. Wojtkowski, "High-speed optical coherence tomography: basics and applications," Appl. Opt. **49**(16), D30–D61 (2010).
5. A. M. Zysk, F. T. Nguyen, A. L. Oldenburg, D. L. Marks, and S. A. Boppart, "Optical coherence tomography: a review of clinical development from bench to bedside," J. Biomed. Opt. **12**(5), 051403 (2007).
6. S. Marschall, B. Sander, M. Mogensen, T. M. Jørgensen, and P. E. Andersen, "Optical coherence tomography-current technology and applications in clinical and biomedical research," Anal. Bioanal. Chem. **400**(9), 2699–2720 (2011).
7. P. H. Tomlins and R. K. Wang, "Theory, developments and applications of optical coherence tomography," J. Phys. D Appl. Phys. **38**(15), 2519–2535 (2005).
8. C. Balas, "Review of biomedical optical imaging–a powerful, non-invasive, non-ionizing technology for improving *in vivo* diagnosis," Meas. Sci. Technol. **20**(10), 104020 (2009).
9. S. Tang, T. B. Krasieva, Z. Chen, and B. J. Tromberg, "Combined multiphoton microscopy and optical coherence tomography using a 12-fs broadband source," J. Biomed. Opt. **11**(2), 020502 (2006).

#212012 - $15.00 USD Received 13 May 2014; revised 6 Jul 2014; accepted 9 Jul 2014; published 15 Jul 2014

10. L. An, P. Li, T. T. Shen, and R. K. Wang, "High speed spectral domain optical coherence tomography for retinal imaging at 500,000 A-lines per second," Biomed. Opt. Express **2**(10), 2770–2783 (2011).
11. L. An, P. Li, G. Lan, D. Malchow, and R. K. Wang, "High-resolution 1050 nm spectral domain retinal optical coherence tomography at 120 kHz A-scan rate with 6.1 mm imaging depth," Biomed. Opt. Express **4**(2), 245–259 (2013).
12. S. Ishida, N. Nishizawa, T. Ohta, and K. Itoh, "Ultrahigh-resolution optical coherence tomography in 1.7 μm region with fiber laser supercontinuum in low-water-absorption samples," Appl. Phys. Express **4**(5), 052501 (2011).
13. K. Zhang and J. U. Kang, "Real-time intraoperative 4D full-range FD-OCT based on the dual graphics processing units architecture for microsurgery guidance," Biomed. Opt. Express **2**(4), 764–770 (2011).
14. S. H. Yun, C. Boudoux, G. J. Tearney, and B. E. Bouma, "High-speed wavelength-swept semiconductor laser with a polygon-scanner-based wavelength filter," Opt. Lett. **28**(20), 1981–1983 (2003).
15. T.-H. Tsai, B. Potsaid, Y. K. Tao, V. Jayaraman, J. Jiang, P. J. S. Heim, M. F. Kraus, C. Zhou, J. Hornegger, H. Mashimo, A. E. Cable, and J. G. Fujimoto, "Ultrahigh speed endoscopic optical coherence tomography using micromotor imaging catheter and VCSEL technology," Biomed. Opt. Express **4**(7), 1119–1132 (2013).
16. M. A. Choma, M. V. Sarunic, C. Yang, and J. A. Izatt, "Sensitivity advantage of swept source and Fourier domain optical coherence tomography," Opt. Express **11**(18), 2183–2189 (2003).
17. J. M. Ridgway, W. B. Armstrong, S. Guo, U. Mahmood, J. Su, R. P. Jackson, T. Shibuya, R. L. Crumley, M. Gu, Z. Chen, and B. J.-F. Wong, "*In vivo* optical coherence tomography of the human oral cavity and oropharynx," Arch. Otolaryngol. Head Neck Surg. **132**(10), 1074–1081 (2006).
18. C.-K. Lee, T.-T. Chi, C.-T. Wu, M.-T. Tsai, C.-P. Chiang, and C. C. Yang, "Diagnosis of oral precancer with optical coherence tomography," Biomed. Opt. Express **3**(7), 1632–1646 (2012).
19. I. Grulkowski, J. K. Nowak, K. Karnowski, P. Zebryk, M. Puszczewicz, J. Walkowiak, and M. Wojtkowski, "Quantitative assessment of oral mucosa and labial minor salivary glands in patients with Sjögren's syndrome using swept source OCT," Biomed. Opt. Express **5**(1), 259–274 (2014).
20. P. Wilder-Smith, K. Lee, S. Guo, J. Zhang, K. Osann, Z. Chen, and D. Messadi, "*In vivo* diagnosis of oral dysplasia and malignancy using optical coherence tomography: preliminary studies in 50 patients," Lasers Surg. Med. **41**(5), 353–357 (2009).
21. U. Mahmood, J. Ridgway, R. Jackson, S. Guo, J. Su, W. Armstrong, T. Shibuya, R. Crumley, Z. Chen, and B. Wong, "*In vivo* optical coherence tomography of the nasal mucosa," Am. J. Rhinol. **20**(2), 155–159 (2006).
22. S.-H. Kim, N. H. Cho, K. Kim, J. S. Lee, B. S. Koo, J. H. Kim, J. H. Chang, and E. C. Choi, "Correlations of oral tongue cancer invasion with matrix metalloproteinases (MMPs) and vascular endothelial growth factor (VEGF) expression," J. Surg. Oncol. **93**(4), 330–337 (2006).
23. P. H. Corrêa, L. C. C. Nunes, A. C. B. R. Johann, M. C. Aguiar, R. S. Gomez, and R. A. Mesquita, "Prevalence of oral hemangioma, vascular malformation and varix in a Brazilian population," Braz. Oral Res. **21**(1), 40–45 (2007).
24. M. Astekar, A. Joshi, G. Ramesh, and R. Metgud, "Expression of vascular endothelial growth factor and microvessel density in oral tumorigenesis," J. Oral Maxillofac. Pathol. **16**(1), 22–26 (2012).
25. Y.-S. Fu and K. H. Perzin, "Non-epithelial tumors of the nasal cavity, paranasal sinuses, and nasopharynx: A clinicopathologic study. I. General Features and Vascular Tumors," Cancer **33**(5), 1275–1288 (1974).
26. P. Wilder-Smith, M. J. Hammer-Wilson, J. Zhang, Q. Wang, K. Osann, Z. Chen, H. Wigdor, J. Schwartz, and J. Epstein, "*In vivo* imaging of oral mucositis in an animal model using optical coherence tomography and optical Doppler tomography," Clin. Cancer Res. **13**(8), 2449–2454 (2007).
27. L. L. Otis, D. Piao, C. W. Gibson, and Q. Zhu, "Quantifying labial blood flow using optical Doppler tomography," Oral Surg. Oral Med. Oral Pathol. Oral Radiol. Endod. **98**(2), 189–194 (2004).
28. S. G. Proskurin, Y. He, and R. K. Wang, "Determination of flow velocity vector based on Doppler shift and spectrum broadening with optical coherence tomography," Opt. Lett. **28**(14), 1227–1229 (2003).
29. A. Mariampillai, B. A. Standish, E. H. Moriyama, M. Khurana, N. R. Munce, M. K. K. Leung, J. Jiang, A. Cable, B. C. Wilson, I. A. Vitkin, and V. X. D. Yang, "Speckle variance detection of microvasculature using swept-source optical coherence tomography," Opt. Lett. **33**(13), 1530–1532 (2008).
30. H. C. Hendargo, R. P. McNabb, A.-H. Dhalla, N. Shepherd, and J. A. Izatt, "Doppler velocity detection limitations in spectrometer-based versus swept-source optical coherence tomography," Biomed. Opt. Express **2**(8), 2175–2188 (2011).
31. H. Ren, Y. Wang, J. S. Nelson, and Z. Chen, "Power optical Doppler tomography imaging of blood vessel in human skin and M-mode Doppler imaging of blood flow in chick chrioallantoic membrane," Proc. SPIE **4956**, 225–231 (2003).
32. X. Li, and H. Ren, "Clutter rejection filters for optical Doppler tomography," US Patent 20070216908.
33. H. Ren, T. Sun, D. J. MacDonald, M. J. Cobb, and X. Li, "Real-time *in vivo* blood-flow imaging by moving-scatterer-sensitive spectral-domain optical Doppler tomography," Opt. Lett. **31**(7), 927–929 (2006).
34. H. Ren and X. Li, "Clutter rejection filters for optical Doppler tomography," Opt. Express **14**(13), 6103–6112 (2006).
35. R. K. Wang, S. L. Jacques, Z. Ma, S. Hurst, S. R. Hanson, and A. Gruber, "Three dimensional optical angiography," Opt. Express **15**(7), 4083–4097 (2007).
36. R. K. Wang and S. Hurst, "Mapping of cerebro-vascular blood perfusion in mice with skin and skull intact by Optical Micro-AngioGraphy at 1.3 mum wavelength," Opt. Express **15**(18), 11402–11412 (2007).

#212012 - $15.00 USD Received 13 May 2014; revised 6 Jul 2014; accepted 9 Jul 2014; published 15 Jul 2014

37. L. An, J. Qin, and R. K. Wang, "Ultrahigh sensitive optical microangiography for *in vivo* imaging of microcirculations within human skin tissue beds," Opt. Express **18**(8), 8220–8228 (2010).
38. R. K. Wang, L. An, P. Francis, and D. J. Wilson, "Depth-resolved imaging of capillary networks in retina and choroid using ultrahigh sensitive optical microangiography," Opt. Lett. **35**(9), 1467–1469 (2010).
39. M. S. Mahmud, D. W. Cadotte, B. Vuong, C. Sun, T. W. H. Luk, A. Mariampillai, and V. X. D. Yang, "Review of speckle and phase variance optical coherence tomography to visualize microvascular networks," J. Biomed. Opt. **18**(5), 050901 (2013).
40. J. Enfield, E. Jonathan, and M. Leahy, "*In vivo* imaging of the microcirculation of the volar forearm using correlation mapping optical coherence tomography (cmOCT)," Biomed. Opt. Express **2**(5), 1184–1193 (2011).
41. C. Blatter, J. Weingast, A. Alex, B. Grajciar, W. Wieser, W. Drexler, R. Huber, and R. A. Leitgeb, "*In situ* structural and microangiographic assessment of human skin lesions with high-speed OCT," Biomed. Opt. Express **3**(10), 2636–2646 (2012).
42. Y. Watanabe, Y. Takahashi, and H. Numazawa, "Graphics processing unit accelerated intensity-based optical coherence tomography angiography using differential frames with real-time motion correction," J. Biomed. Opt. **19**(2), 021105 (2014).
43. B. Davoudi, A. Lindenmaier, B. A. Standish, G. Allo, K. Bizheva, and A. Vitkin, "Noninvasive *in vivo* structural and vascular imaging of human oral tissues with spectral domain optical coherence tomography," Biomed. Opt. Express **3**(5), 826–839 (2012).
44. B. Davoudi, M. Morrison, K. Bizheva, V. X. D. Yang, R. Dinniwell, W. Levin, and I. A. Vitkin, "Optical coherence tomography platform for microvascular imaging and quantification: initial experience in late oral radiation toxicity patients," J. Biomed. Opt. **18**(7), 076008 (2013).
45. W. J. Choi, R. Reif, S. Yousefi, and R. K. Wang, "Improved microcirculation imaging of human skin *in vivo* using optical microangiography with a correlation mapping mask," J. Biomed. Opt. **19**(3), 036010 (2014).
46. W. J. Choi, H. Wang, and R. K. Wang, "Optical coherence tomography microangiography for monitoring the response of vascular perfusion to external pressure on human skin tissue," J. Biomed. Opt. **19**(5), 056003 (2014).
47. http://www.thorlabs.us/newgrouppage9.cfm?objectgroup_id=6473&pn=OCS1310V1.
48. I. Grulkowski, J. J. Liu, B. Potsaid, V. Jayaraman, C. D. Lu, J. Jiang, A. E. Cable, J. S. Duker, and J. G. Fujimoto, "Retinal, anterior segment and full eye imaging using ultrahigh speed swept source OCT with vertical-cavity surface emitting lasers," Biomed. Opt. Express **3**(11), 2733–2751 (2012).
49. Laser Institute of America, American National Standard for Safe Use of Lasers ANSI Z136.1-2000," American National Standards Institute Inc., New York, NY (2000).
50. J. Fingler, R. J. Zawadzki, J. S. Werner, D. Schwartz, and S. E. Fraser, "Volumetric microvascular imaging of human retina using optical coherence tomography with a novel motion contrast technique," Opt. Express **17**(24), 22190–22200 (2009).
51. G. A. Scardina and P. Messina, "Hashimoto's thyroiditis: lingual and labial capillary microcirculation in patients affected by macroglossia," Int. J. Morphol. **25**(2), 411–416 (2007).
52. R. Djaberi, J. D. Schuijf, E. J. de Koning, D. C. Wijewickrama, A. M. Pereira, J. W. Smit, L. J. Kroft, A. Roos, J. J. Bax, T. J. Rabelink, and J. W. Jukema, "Non-invasive assessment of microcirculation by sidestream dark field imaging as a marker of coronary artery disease in diabetes," Diab. Vasc. Dis. Res. **10**(2), 123–134 (2013).
53. R. V. Krstič, *Human Microscopic Anatomy: An Atlas for Students of Medicine and Biology* (Springer-Verlag, Berlin, 1991).
54. E. A. Naumova, T. Dierkes, J. Sprang, and W. H. Arnold, "The oral mucosal surface and blood vessels," Head Face Med. **9**(1), 8 (2013).

1. Introduction

Diseases in human cavities such as mouth and nose are a prevalent and significant health care problem worldwide. For instance, it is estimated that 42,440 new cancer cases would occur in the oral cavity and pharynx in 2014, accounting for over 2.5% of all cancers in United States [1]. Particularly for under-privileged groups in the developed or developing countries, the cavity-related diseases have been one of the most important health burdens in terms of their prevalence, severity and associated healthcare cost [2,3]. Apart from low public awareness of the diseases, current visual examination by physicians has limited opportunity to manage the diseases at early stage because of subjective criteria of the examiners. Accordingly, necessity for an effective diagnostic tool has been on high demand for prognosis, diagnosis and early-treatment of the cavity diseases.

Optical coherence tomography (OCT) has attracted much attention as a noninvasive optical modality in the realm of biomedical imaging because of its micrometer resolution and appreciable imaging depth, high speed, and high sensitivity [4–8]. Recent technical developments in broadband optical light sources, detectors and imaging processing methods have boosted its imaging ability in terms of resolution and speed, permitting rapid volumetric

#212012 - $15.00 USD Received 13 May 2014; revised 6 Jul 2014; accepted 9 Jul 2014; published 15 Jul 2014

scanning of tissue microstructures *in vivo* [9–13]. With the advent of tunable wavelength laser [14], implementation of swept source OCT (SS-OCT) using the laser has led to enhancement in system signal sensitivity and ranging distance, which is important for a wide range of clinical application [15,16]. Over the years, this emerging technology has proven useful in the diagnosis of the cavity disorders through *in vivo* feasibility or clinical studies for human [2,17–21]. These OCT studies have evaluated changes in cavity tissue morphology (e.g., variation of epithelial thickness) and optical properties of backscattered OCT signals from the cavity tissue layers (e.g., degree of standard deviation (SD) of the A-mode scan signal profile) for identification of abnormalities. Statistically significant differences in these multi-parametric values have been found between healthy and diseased tissues within human cavities [2,18,19].

Notwithstanding, there has been limited discussion regarding the assessment of micro vasculature in the human cavity tissues. The microcirculation within cavity tissues would be an invaluable indicator for assessing cavity disorders due to vascular malformation associated with the disease progression [22–25]. Some previous studies indicated the use of optical Doppler tomography (ODT) to detect the functional blood flow within cavity tissue [26,27]. ODT is a functional extension of OCT that measures phase change due to Doppler frequency shift of light backscattered from red blood cells (RBCs) moving through the functional vessel lumen [28]. The phase difference between successive depth scans (A-lines) is used to calculate blood flow parallel to the imaging direction, representing existence of the vessel. However, the conventional ODT has difficulty to map complex microvascular network innervating the tissue because of its Doppler angle dependency on the imaging direction [29] and its low sensitivity to slow flows, particularly capillary flow [30]. To reduce the difficulty of the direct use of Doppler phases to evaluate blood flow, Ren et al was the first to introduce a concept of using power Doppler to image moving scatterers within tissue [31,32], in which the intensity OCT signals were band-pass filtered to achieve the goal [31–34]. The method is important because it indicates the intensity OCT signals can be used to locate the Doppler information, thus enhancing the ODT's ability to image functional blood flows.

Recently, OCT-based microangiography to map functional blood flow within tissue has been demonstrated by complex OCT signals [35–38], and later by the speckle variance [29,39–42] of OCT signals. The speckle variance approach essentially utilizes the fluctuation of the OCT intensity or magnitude signals, i.e. temporal speckle dynamics, to contrast the functional blood flow. Dynamic speckle signals are rapidly decorrelated due to moving RBCs whereas the speckle fluctuation is relatively less evident in the surrounding tissues. This speckle de-correlation gives opportunity to contrast the blood flow within living tissues by calculating speckle variation between consecutive A-scans or B-frames, with the latter having enough sensitivity to detect slow flows [29, 39, 40]. Several intensity-based algorithms for vessel extraction have used amplitudesof the OCT signals emanating from vascular tissue beds, showing potential to obtain three-dimensional (3D) tissue perfusion map *in vivo* [37–42]. Very recently, there is interest in imaging oral cavity vasculatures using the speckle variance OCT (svOCT), one of the intensity-based OCT angiography methods [43,44]. Although this method has been demonstrated to have ability to visualize network that is made up of big blood vessels, little information on the microvessels has been provided [43,44].

To successfully obtain the microvasculature within cavity tissues, the existing methods may be limited by two main factors: (1) lack of proper probe to image tubular-shaped or lateral structures inside the cavity. So far, most of the cavity vascular works have been conducted using the forward viewing OCT probes, which restrict its use to only visible part of the human mouth such as a labial tissue. (2) The presence of strong residual signals arising from the static tissues, which reduces the contrast to background ratio in the vascular images. To mitigate the problem of the noise background, we recently proposed a new intensity-based OCT angiography to reduce the static artifacts in the angiogram, allowing for the enhanced ability to visualize the tissue microvessel networks compared to the other existing OCT

#212012 - $15.00 USD Received 13 May 2014; revised 6 Jul 2014; accepted 9 Jul 2014; published 15 Jul 2014

angiographies [45,46]. Its microvascular imaging ability has been successfully demonstrated with the several human skin tissue beds *in vivo* [45,46].

In this paper, we present 3D vascular imaging of living human cavity tissues using the modified OCT microangiography method. To do so, two types of probe attachments for forward and side view imaging are devised and incorporated into a single OCT probe to selectively access to the overall cavity tissue sites. Healthy oral cavity and nasal cavity tissues are explored with the proposed instrument to obtain microvasculatures as well as tissue microstructures. To our best knowledge, this is the first OCT angiography study for revealing vascular anatomy of the wide-range of oral and nasal human cavity tissues *in vivo*.

2. Material and method

2.1 Swept-source OCT (SS-OCT) instrument

Imaging was performed using a prototype 1300 nm SS-OCT system along with a handheld probe acquired from the Thorlabs research labs. A photograph of the SS-OCT system used in this study is shown in Fig. 1. The system consisted of four separate main components: a swept-source engine, an imaging module, a probe, and a workstation. The whole system was mounted on a wheeled cart to facilitate its portability for clinical use. In Fig. 1(a), the swept-source engine contained a MEMS-tunable vertical cavity surface-emitting laser (VCSEL, SL1310V1-10048, Thorlabs Inc.) as the OCT light source. This VCSEL source is able to sweep the lasing wavelength across a broad spectral range near 1300 nm at a fixed repetition rate of 100 kHz, giving a long coherence length (≥50 mm) and an extended imaging range (nominally ~12 mm) [47,48]. The 28 mW output beam exiting from the VCSEL laser was fiber-coupled into a Mach-Zehnder interferometer built in the imaging module, where the light was evenly split into two beams by a 50:50 broadband fiber coupler that were directed to a reference arm and a sample arm, respectively. The sample arm was terminated in the probe consisting of an imaging head (including a fiber collimator and X-Y galvanometric scanners) and a 5 × telecentric objective lens (LSM03, working distance = 25.1 mm, Thorlabs Inc.), allowing for the light delivery to and collection from the sample. The optical power of incident light upon the sample was ~5.2 mW well below the American National Standards Institute (ANSI) standards (Z136.1) for the safe use of near infrared light at 1310 nm [49].

For the oral cavity imaging, the probe was horizontally mounted on a manual positioning stage shown in Fig. 1(b) as a photograph, in which location of the probe can be freely adjusted in lateral direction. The stage included a head frame with a forehead rest and a chin rest to restrict involuntary head movement during the cavity imaging. For the nasal cavity imaging, the probe was mounted on an adjustable articulated arm as shown in Fig. 1(c), making it flexible to approach the nasal tract. The interface of the probe was modified with home-made but disposable probe attachments to provide an easy access for the probing beam to the cavity tissues. The axial scan (A-lines) in depth was performed by sweeping the laser wavelength at 100 kHz and the transverse scan (B-frame) was achieved by scanning laterally the galvanometric scanners in the imaging probe head. Light backscattered from the sample was recombined with reflected light from the reference arm in the imaging module and then the resulting interference signal was detected by a gain-balanced photo-detector, allowing cancellation of DC and autocorrelation terms. The detector photocurrents were sampled by a 12 bits A/D data acquisition card at a 500 MSPS sampling rate, yielding a raw fringe signal with 4096 pixels for an A-line. All imaging processes including data acquisition were managed by a 64 bit workstation (T5600, six cores 2.3 GHz, 32 GB DDR3 RAM, Dell).

#212012 - $15.00 USD Received 13 May 2014; revised 6 Jul 2014; accepted 9 Jul 2014; published 15 Jul 2014

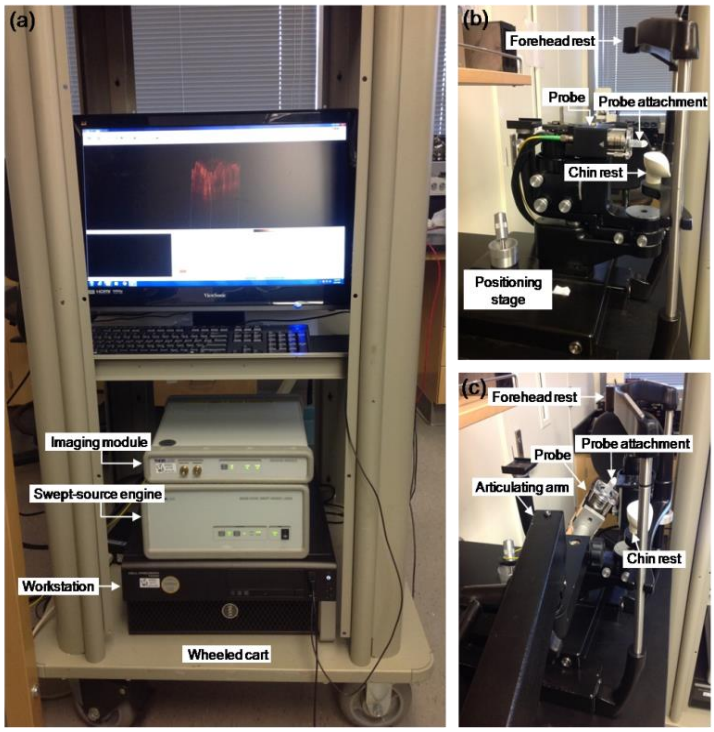

Fig. 1. Photographs of the swept-source OCT (SS-OCT) system for human cavity imaging. (a) Portable benchtop SS-OCT system on the wheeled cart, (b) Probe stage for oral cavity imaging, (c) Probe stage for nasal cavity imaging.2.2 Probe attachment design for side/forward imaging of the cavity tissues

In order to allow for the light beam to access different sites in the cavities, we customized the probe with two types of disposable probe attachments to achieve two scan modes on the single probe platform: side imaging and forward imaging. The side-viewing probe attachment is necessary for imaging circumferential or lateral wall tissue regions inside the cavities such as buccal mucosa or nasal mucosa, whereas the forward-viewing probe attachment is useful for imaging frontal regions inside the cavity such as labial mucosa. Figures 2(a) and 2(d) are schematics of the devised OCT probe attachments for side-view imaging and forward-view imaging, respectively. In Fig. 2(a), the side-viewing probe attachment was consisted of a sterilized 27-mm-long semi-transparent plastic tube (10 mm outer diameter) with a 5 mm × 5 mm square window, where a silver-coated right-angled prism mirror (MRA05-P01, 5 mm length, ≥97.5% reflectance at 1.3 μm, Thorlabs Inc.) was glued on the surface of the tube head cap (7 mm length) for near normal reflection (~90°) of the light from the objective lens. Since the coated surface of the mirror (hypotenuse) was centered below the window of the tube, the probe light was able to be laterally scanned through the window (Fig. 2(a)).

For the forward-viewing probe attachment, we employed a disposable 5-mm-diameter plastic aural speculum (Fig. 2(d)) that is a distal attachment of an optoscope to examine inner structures of the ear. Commonly, both probe attachments were fit into a rubber ring and fixed in a 25-mm-diameter hole of a transparent plastic plate, where metal plates on bottom of the plastic plate gave their support. The plastic plate was affixed to two adjustable aluminum space bars connected to the imaging head of the probe. The spacer bars maintained a constant distance between the objective lens and the tissue to be imaged. Because the probe attachments are detachable from the probe, it is possible to properly choose the imaging mode for a given cavity region. In addition, the attachments can be easily disposed after the imaging and replaced with new ones to keep the probe hygienic. The probes integrated each probe

#212012 - $15.00 USD Received 13 May 2014; revised 6 Jul 2014; accepted 9 Jul 2014; published 15 Jul 2014

attachment are shown in Figs. 2(b) and 2(e). With the attachments, the probing scanning is confirmed through trace of an aiming laser beam (630 nm) as Figs. 2(c) and 2(f).

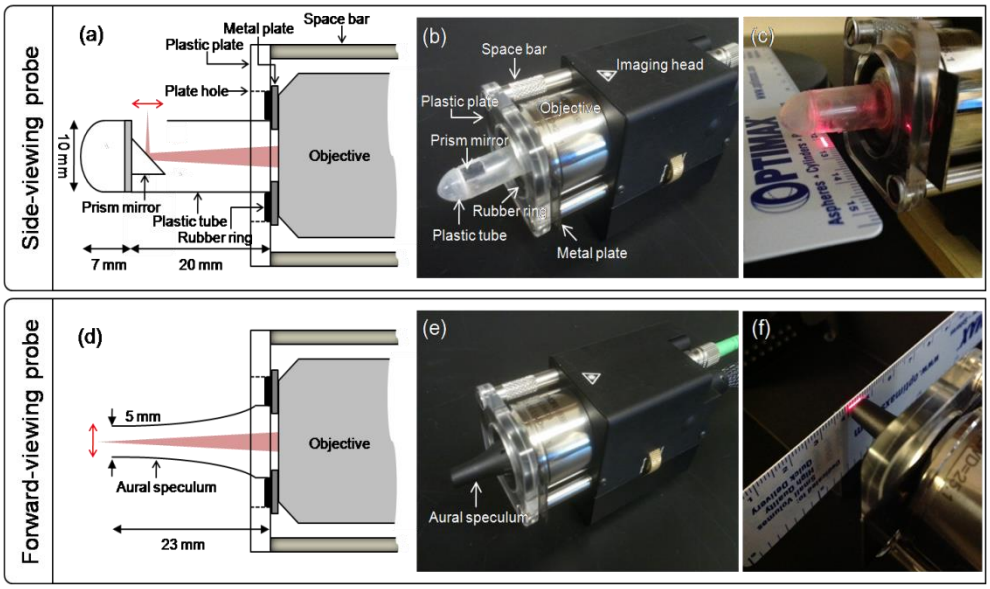

Fig. 2. OCT probe design for imaging the cavity tissues. (a) and (d) Illustration of the probe attachments for side-viewing and forward-viewing imaging, respectively. (b) and (e) Pictures of the probes incorporated each probe attachment, (a) and (d). (c) and (f) photographed scanning beam pattern using the side-viewing probe and the forward-viewing probe, respectively

2.3 Characterization of the system performance

To test the system performance, several parameters were characterized with the SS-OCT instrument with the side-viewing probe configuration. Figure 3(a) shows an optical spectrum of the probe output measured using an optical spectrum analyzer (MS9710B, Anritsu), for which a full width at half maximum (FHWM) of the spectrum curve was estimated to be about 67.57 nm. In order to measure the system sensitivity, we obtained A-line signals from a well-calibrated 40 dB attenuator in a sample arm along different optical delay of the reference arm. The recorded fringe signals were Fourier transformed and represented as point spread functions (PSFs). The sensitivity was calculated as the ratio of the PSF peak to the standard deviation of the noise floor that was measured while the sample arm was blocked [16]. The resulting sensitivity profiles at the different imaging depth were represented as a logarithmic scale in Fig. 3(b), showing that the sensitivities (peak intensity) are relatively constant, where there is only ~1 dB measurable drop from the average sensitivity of 105 dB over 4.25 mm imaging range. This indicates that the OCT system is able to image the tissue located at a large ranging distance without significant sensitivity roll-off drop. FWHMs of the PSF amplitudes were measured at the different imaging depth as Fig. 3(c) and their average was about 20.9 μm, corresponding to an axial resolution of the system in air (15.1 μm in the tissue). To measure the lateral resolution, we performed 3D OCT imaging of a U.S. Air Force (USAF) test target with positive patterns on glass (Edmund Optics Inc.) and produced an *en face* image of the top surface of the USAF target from the acquired 3D OCT data set in Fig. 3(d). The smallest resolvable lines in the image were taken as an intensity profile (inset) with a distance gap of 22 μm between the line pair, which was estimated as the lateral resolution of the system [43].

#212012 - $15.00 USD Received 13 May 2014; revised 6 Jul 2014; accepted 9 Jul 2014; published 15 Jul 2014

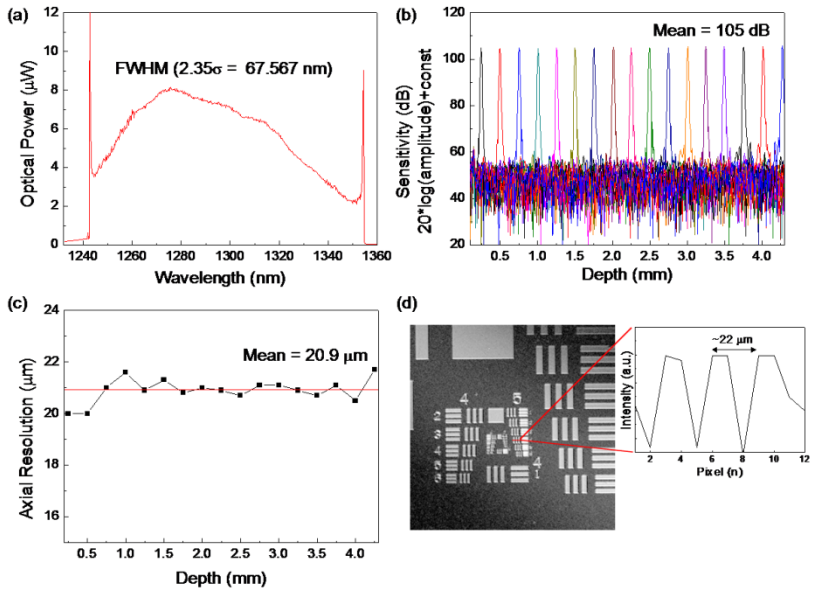

Fig. 3. (a) Optical spectrum of the probe output of the VCSEL SS-OCT system. (b) Logarithmic plot of the measured sensitivity profiles (divided the PSF by the standard deviation of noise floor) against the different imaging depth. Sensitivity reduction is negligible up to depth of 4.25 mm in air. (c) Free space axial resolution values defined as FWHM of the PSF amplitudes with the imaging depth. Horizontal line indicates the mean value of 20.9 μm. (d) *En face* OCT image of top surface of the 1951 USAF test target. From an intensity line profile (solid line in the image), a fair of lines with a distance gap of 22 μm are recognizable, corresponding to the lateral resolution of the system.

2.4 Data acquisition and vascular mapping process

For vascular mapping of the cavity tissues, we adopted a new intensity-based OCT angiographic technique that was lately developed in our group [45]. The method utilizes the algorithms of ultrahigh-sensitive optical microangiography (UHS-OMAG) [37,38] and correlation mapping OCT (cmOCT) [40] where the vessel extraction is achieved with the combination of two angiograms obtained from each algorithm with the same OCT data set. The method was described in detail in the previous paper [45], and only a brief overview is provided here. 3D OCT imaging was performed on the cavity tissue region of 2 mm (X) × 2 mm (Y) using raster scanning of the galvanometric scanners. For fast B-scan (in X direction), a B-frame contained 256 A-lines at an imaging rate of 100 frames/s (FPS). In the slow C-scan (in elevational Y direction), total of 2048 B-frames were captured with 8 repetitions at the each location. Once the scan was completed, one OCT data cube (256 (X) × 2048 (Y) × 4096 (Z) voxels) was produced over the region of interest within 20 s. After the analytical OCT data cube was converted to an amplitude form using a fast Fourier transformation (FFT), a cross-correlation based image registration method was applied for the adjacent B-frames in the 3D amplitude data set to compensate axial displacement induced by possible tissue bulk motion [50]. Then, subtraction between the adjacent B-frames was operated with the consecutive 8 B-frames obtained at the same location to suppress the stationary signals and extract the moving blood flow signals, and thus the resulting 7 images were averaged to enhance flow signal sensitivity, yielding one cross-sectional blood flow intensity image. The inter-frame subtraction (high-pass filtering) and averaging are similar to the UHS-OMAG process [37], except for use of the amplitude values instead of the complex values in the OCT signals (here, we call the flow intensity image as intensity-based OMAG (IB-OMAG) image).

#212012 - $15.00 USD Received 13 May 2014; revised 6 Jul 2014; accepted 9 Jul 2014; published 15 Jul 2014

As computing along the slow scan direction, total 256 cross-sectional (XZ) IB-OMAG images (256 (X) × 2048 (Z) pixels) were obtained from the 3D amplitude data set.

Meanwhile, the flow intensity image with the amplitude difference may contain residual signals arising from the surrounding static tissues, comparable to or larger than the flow signals in strength for highly-scattered tissues, which is responsible for degradation in the flow sensitivity. In order to remove the static artifacts, we obtained additional 3D flow intensity images by applying the cmOCT [40] to the same 3D amplitude data set. The cmOCT is based on a normalized cross-correlation (NCC) between the adjacent B-frames to map the flow, in which small absolute values of the correlation reflect the blood flow and large positive ones indicate the static tissues [40]. Thus, a proper thresholding (depending on the degree of correlation) to the correlation map is able to filter out the static component in the map, creating one cmOCT image. In this work, the cmOCT image was used as a mask on the IB-OMAG image. From the obtained 256 cmOCT images, each cmOCT image was binarized and then multiplied with the corresponding IB-OMAG image, allowing suppression of the static artifacts in the IB-OMAG image [45]. Eventually, the 256 masked IB-OMAG (termed mOMAG) images were reconstructed. The post data processing was performed with a laboratory-software written by a MATLAB language (R2011b, MathWorks, Inc.) on the workstation and a total computation time took within 10 minutes. The microvessel network was displayed as an *en face* (XY) view of the 3D rendered vasculature which was reconstructed using the 3D mOMAG data set through an image rendering software (AMIRA 5.3.2, Visage Imaging). To remove breathing or pulsation induced stripe patterns on the *en face* image, a FFT-based low-pass filtering was properly processed to the *en face* image.

3. Experimental results

3.1 Structural and vascular imaging of the oral cavity tissues

OCT imaging of various cavity tissue regions of a healthy male volunteer was performed to demonstrate feasibility of *in vivo* 3D cavity microangiography. First, we investigated the microcirculation within a lower lip of the oral cavity tissues. The volunteer seated in a temperature controlled room with a temperature of approximately 23 °C and the head was gently placed between the chin rest and the forehead rest (Fig. 1(b)). The forward-viewing attachment was installed to the imaging probe and approached forward to the lower lip using the movable positioning stage. The probe beam spot was located on the sample surface which could be identified from a well-focused view during monitoring B-mode OCT imaging at 100 FPS. Figure 4(a) is a 3D rendered OCT structural image of the scanned portion of lower lip with the 3D mOMAG data (yellow) overlay. Representative cross-sections of the structure and the mOMAG data (2.0 mm (X) × 1.35 mm (Z)) at a position (indicated as a black box) in Fig. 4(a) are shown in Figs. 4(b) and 4(c) with gray scale intensities, respectively. The structural image (Fig. 4(b)) describes typical labial anatomical features; an epithelial layer (EP) and an underlying lamina propria (LP). The corresponding mOMAG image (Fig. 4(c)) indicates labial blood perfusion in the functional vessels. The overlay of the mOMAG data (red) on the structural image (Fig. 4(d)) shows location of the blood vessels in the LP, making a clear demarcation from the avascular EP region. To visualize vessel networks in depth, the 3D mOMAG data sets taken over different depths of 253 μm and 407 μm below the surface were reduced to 2D *en face* (XY) images and shown in Figs. 4(e) and 4(f), respectively. Black bars in Fig. 4(a) indicate depths for Figs. 4(e) and 4(f). In Fig. 4(e), abundant hairpin-like capillary loops (arrow heads) are visible nearby the junction of the EP and the LP where they are arranged in parallel to the labial tissue surface. Note that the capillaries in the angiogram may appear to be blurred because of the limited lateral resolution (22 μm) in current work. However, as long as the spacing between the capillaries is more than 22 μm (which is usually true for most microcirculatory tissue beds), our technique would be able to differentiate them. At the deeper depth (Fig. 4(f)), it is observed that the capillaries were emerged from wider

#212012 - $15.00 USD Received 13 May 2014; revised 6 Jul 2014; accepted 9 Jul 2014; published 15 Jul 2014

planar arterioles (arrows). The labial capillary networks in the healthy subject may be provided well with noninvasive 2D angiography techniques (capillaroscopy [51] and sidestream darkfield microscopy [52]), which, however, could not provide depth-resolved microvasculatures. The labial microcirculation in depth is also illustrated in a movie clip (Media 1).

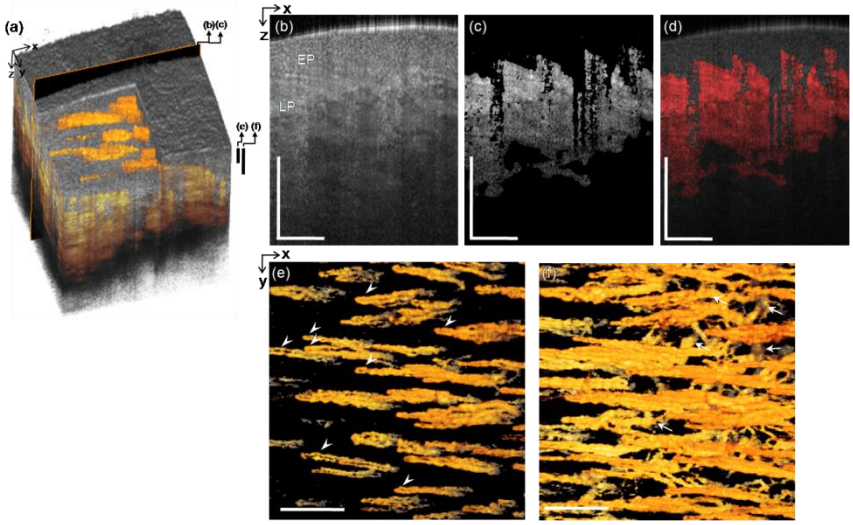

Fig. 4. *In vivo* microvascular imaging of the lower lip of healthy volunteer with the forward-viewing probe. (a) 3D rendered OCT structural image with the 3D mOMAG data (yellow) overlay. (b) and (c) Representative cross-sectional structural and mOMAG images (2.0 mm (X) × 1.35 mm (Z)) at a position (a black box) in (a), respectively. (d) Overlay of the mOMAG image (red) on the structural image. EP: epithelium, LP: lamina propria. (e) and (f) 2D *en face* views (2.0 mm (X) × 2.0 mm (Y)) of the 3D mOMAG data volumes taken over depths of 253 μm and 407 μm from the surface, respectively. Black bars in (a) are the depth ranges for (e) and (f). Arrow heads in (e) indicate hairpin-like capillary loops emerged from the arterioles (arrows) in (f). A fly-through image of the microvasculature is shown with a movie clip (Media 1). Scale bars: 0.5 mm.

Furthermore, microvasculature of a tongue was imaged with the forward-viewing probe. In doing so, the attachment was advanced to the dorsal surface of the tongue for stable OCT imaging. Figure 5(a) shows a 3D rendered OCT structural image of apex (tip) of the dorsal tongue with the 3D mOMAG data (yellow) overlay. Representative structural and vascular cross-sections (2.0 mm (X) × 1.66 mm (Z)) taken at a position (a black box) in Fig. 5(a) are shown as Fig. 5(b) and 5(c), respectively. Figure 5(b) shows a lingual anatomy including epithelial layer (EP), connective tissue (CT), lamina propria (LP), and specific two types of lingual papillae: fungiform papillae (FuP) and filiform papillae (FiP) that give a characteristic rough texture on the upper surface of the tongue [53]. Blood perfusion in the lingual structure is depicted with the mOMAG image in Fig. 5(c). The structure with the mOMAG data (red) overlay in Fig. 5(d) identifies location of the vessels in the CT of the individual papillae. Figures 5(e) and 5(f) are 2D *en face* (XY) images of the 3D vasculatures taken over depths of 434 μm and 692 μm below the surface of the dorsal tongue, respectively. Unique vascular appearances were found in the FuP and the FiP: namely, capillaries are vertically oriented to the surface of the dorsal tongue and grouped with separate loops within the individual lingual papillae. However, the FiPs have one or a few capillary loops (arrows) whereas the capillary loops in the FuPs (asterisks) were more densely packed and wider in area than the FiPs, which were interspaced amongst the FiP capillaries. This vascular arrangement was very similar to other angiograms obtained from lateral and middle regions of the dorsal tongue with the system (not shown here) in our experiments and well correlated with the prior results reported

#212012 - $15.00 USD Received 13 May 2014; revised 6 Jul 2014; accepted 9 Jul 2014; published 15 Jul 2014

in literature [54]. The lingual microcirculation in depth is represented with a movie clip (Media 2).

We also imaged other mucosal regions in the mouth, i.e., labial mucosa and buccal (chick) mucosa. For imaging the labial mucosa, a disposable forward-viewing probe attachment was inserted into a space between the lower lip and teeth, and then slightly pressed onto the mucolabial surface to be imaged. Figure 6(a) is an overlay of the 3D OCT structure and the 3D mOMAG data (yellow) of the labial mucosa, in which a black box indicates a location of the structure and the corresponding vasculature cross sections (2.0 mm (X) × 1.6 mm (Z)) as Figs. 6(b) and 6(c), respectively. In Figs. 6(e) and 6(f), microvessel networks of the oral soft tissue were delineated with 2D *en face* (XY) images of the 3D vasculatures taken over depths of 362 μm and 656 μm below the surface, respectively where each depth was indicated as black bars in Fig. 6(a). Dense capillary loops are oriented relatively parallel to the mucolabial surface, of which length is shorter than those of the lower lip in Fig. 4(e). These capillary beds are fed by underlying planar arteriole plexus shown in Fig. 6(f). Depth-resolved microcirculation of the lower lip mucosa is illustrated with a movie clip (Media 3).

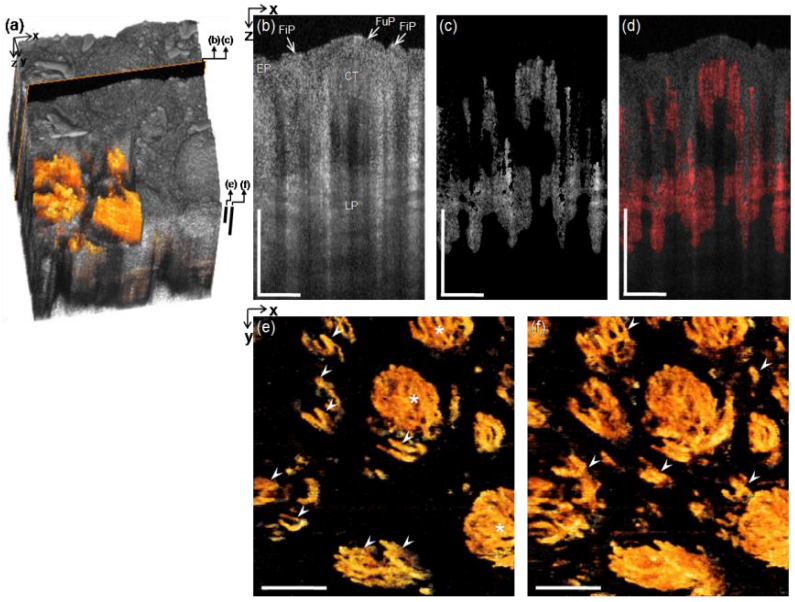

Fig. 5. *In vivo* microvascular imaging at the tongue apex of a healthy volunteer with the forward-viewing probe. (a) 3D rendered OCT structural image with the 3D mOMAG data (yellow) overlay. (b) and (c) Representative cross-sectional structural and mOMAG images (2.0 mm (X) × 1.66 mm (Z)) at a position (a black box) in (a), respectively. (d) Overlay of the mOMAG image (red) on the structural image. EP: epithelium, FuP: fungiform papillae, FiP: filiform papillae, CT: connective tissue, LP: lamina propria. (e) and (f) 2D *en face* views (2.0 mm (X) × 2.0 mm (Y)) of the 3D mOMAG data volumes taken over depths of 434 μm and 692 μm from the surface, respectively. Black bars in (a) are the depth ranges for (e) and (f). Arrow heads in (e) and (f) indicate vertically oriented separate capillary loops in the individual FiPs, which are much narrower and fewer than those of the FuPs (asterisks in (e)). A fly-through image of the microvasculature is shown with a movie clip (Media 2). Scale bars: 0.5 mm.

For the buccal mucosa imaging, the forward-viewing probe attachment was replaced with the side-viewing probe attachment, which allowed for the access to the mucosal wall inside the mouth. To protect the prism mirror in the tube, the opening window was covered with a 120-μm-thick transparent sterilized sheath, resulting in light attenuation of ~0.3 dB through the sheath. Figure 7(a) shows the 3D structure of the buccal mucosa overlaid with the 3D mOMAG data (yellow). The cross sections (2.0 mm (X) × 1.72 mm (Z)) at a position (a black box in Fig. 7(a)) and the corresponding overlay are represented as Figs. 7(b)-7(d),

#212012 - $15.00 USD Received 13 May 2014; revised 6 Jul 2014; accepted 9 Jul 2014; published 15 Jul 2014

respectively. Similar to the labial mucosa, two major tissue layers, the epithelium (EP) and the lamina propria (LP) are distinguished in the buccal mucosa as Fig. 7(b) and existence of the vessels are identified in the LP only as shown in Fig. 7(d). An uppermost layer (SS) and subsequent lower reflective signals in Fig. 7(b) are due to the surface of the sheath wrapped the tube window and the oral secretion, respectively. Depth-resolved microvessel networks are visualized from the 3D vasculatures taken through depths of 461 μm and 588 μm below the surface, showing that the vascularity is quite similar to the microcirculatory bed of the lower lip mucosa in Figs. 6(e) and 6(f) but the capillary loops appear somewhat lengthy than the mucolabial capillaries. These vascular morphology of the oral mucosa sites was favorably consistent with the previous result in *ex vivo* study [54]. Media 4 shows depth-resolved microcirculation of the buccal mucosa tissue.

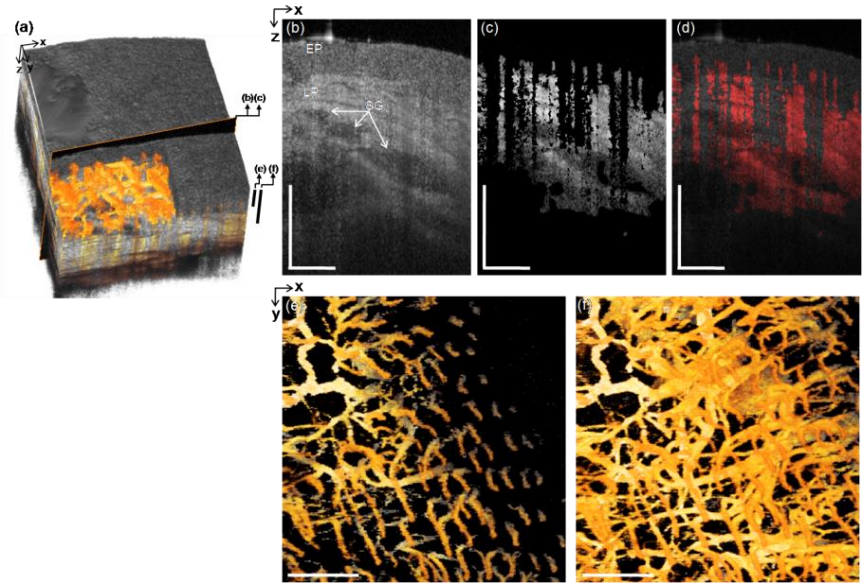

Fig. 6. *In vivo* microvascular imaging of mucosa of the lower lip of a healthy volunteer with the forward-viewing probe. (a) 3D rendered OCT structural image with the 3D mOMAG data (yellow) overlay. (b) and (c) Representative cross-sectional structural and mOMAG images (2.0 mm (X) × 1.6 mm (Z)) at a position (a black box) in (a), respectively. (d) Overlay of the mOMAG image (red) on the structural image. EP: epithelium, LP: lamina propria, SG: salivary gland. (e) and (f) 2D *en face* views (2.0 mm (X) × 2.0 mm (Y)) of the 3D mOMAG data volumes taken over depths of 362 μm and 656 μm from the surface, respectively. Black bars in (a) are the depth ranges for (e) and (f). A fly-through image of the microvasculature is shown with a movie clip (Media 3). Scale bars: 0.5 mm.

3.2 Structural and vascular imaging of the nasal cavity tissue

Finally, *in vivo* microvascular imaging of the nasal cavity was performed with the system. Nasal hairs in the nose were trimmed by the subject with an electric shaver the day before the measurement. The imaging probe with the side-viewing probe attachment mounted on the articulating arm was lightly inserted into the nasal cavity through the nose passage of the subject whose head was immobile by the forehead rest and the chin rest (see Fig. 2(c)). Figure 8(a) shows a 3D OCT structural image of the inferior turbinate in the nasal cavity with the overlaid 3D mOMAG data (yellow). The cross sections (2.0 mm (X) × 1.57 mm (Z)) of the structure and vasculature at the same location (a black box in Fig. 8(a)) are as shown in Figs. 8(b) and 8(c), respectively, where a pseudostratified columnar epithelium (PCE) and an underlying lamina propria (LP) including glandular elements such as a seromucinous duct (SD) were observed in Fig. 8(b), which are the expected structural features of the healthy

#212012 - $15.00 USD Received 13 May 2014; revised 6 Jul 2014; accepted 9 Jul 2014; published 15 Jul 2014

nasal mucosa [21]. The microcirculatory bed in the nasal mucosa (Fig. 8(e)) over depth of 502 µm below the surface revealed an interesting ring-like vascular arrangement. Ruptures across few vessels (arrow heads) are seen in the image, which might be due to beam shading by the untrimmed leaned nasal hairs. As overlaying an *en face* OCT tomogram at 502 µm in depth on the angiogram, it is obvious that the vasculatures encircled around the nasal hairs (arrows) in hair pores, which may be responsible for supplying necessary nutrients to the hair follicles for nasal hair growth. The depth-resolved nasal microcirculation is represented with a movie clip (Media 5).

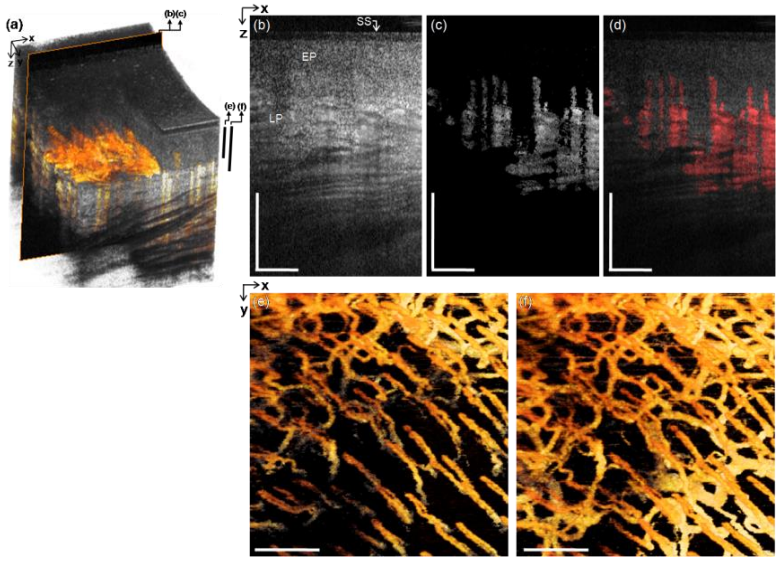

Fig. 7. *In vivo* microvascular imaging of buccal (chick) mucosa of a healthy volunteer with the side-viewing probe. (a) 3D rendered OCT structural image with the 3D mOMAG data (yellow) overlay. (b) and (c) Representative cross-sectional structural and mOMAG images (2.0 mm (X) × 1.72 mm (Z)) at a position (a black box) in (a), respectively. (d) Overlay of the mOMAG image (red) on the structural image. SS: sheath surface, EP: epithelium, LP: lamina propria. (e) and (f) 2D *en face* views (2.0 mm (X) × 2.0 mm (Y)) of the 3D mOMAG data volumes taken over depths of 461 µm and 588 µm from the surface, respectively. Black bars in (a) are the depth ranges for (e) and (f). The vascularity is quite similar to the mucolabial microcirculatory bed in Fig. 6. A fly-through image of the microvasculature is shown with a movie clip (Media 4). Scale bars: 0.5 mm.

#212012 - $15.00 USD Received 13 May 2014; revised 6 Jul 2014; accepted 9 Jul 2014; published 15 Jul 2014

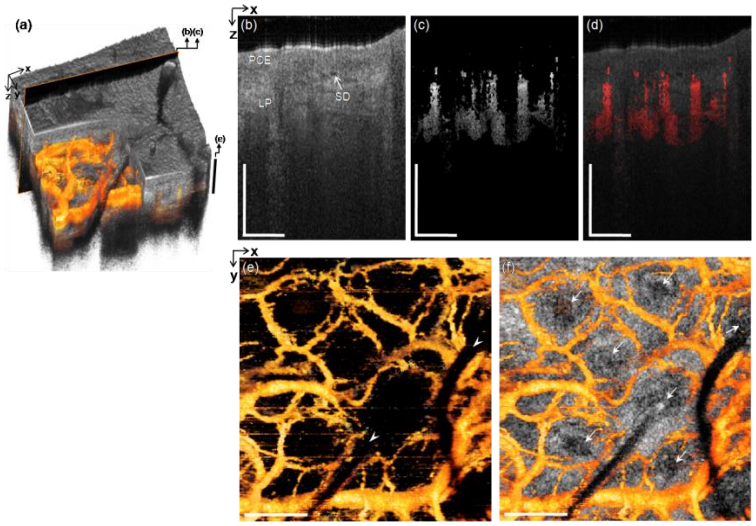

Fig. 8. *In vivo* microvascular imaging of inferior turbinate in nasal cavity of a healthy volunteer with the side-viewing probe. (a) 3D rendered OCT structural image with the 3D mOMAG data (yellow) overlay. (b) and (c) Representative cross-sectional structural and mOMAG images (2.0 mm (X) × 1.57 mm (Z)) at a position (a black box) in (a), respectively. (d) Overlay of the mOMAG image (red) on the structural image. PCE: pseudostratified columnar epithelium, LP: lamina propria, SG: seromucinous duct. (e) 2D *en face* view (2.0 mm (X) × 2.0 mm (Y)) of the 3D mOMAG data volumes taken over depths of 502 μm from the surface, demonstrating vascular characteristics with the ring-like microvasculature. Cut-offs across the vessels (arrow heads) are due to beam shading by the leaned nasal hairs. Black bar in (a) is the depth range for (e). (f) The vasculature with an *en face* OCT tomogram at 502 μm in depth overlay, indicating that each nasal hair in the hair pores (arrows) is surrounded by ring-like vessels, possibly feeding nutrients for the hair growth. A fly-through image of the microvasculature is shown with a movie clip (Media 5). Scale bars: 0.5 mm.

4. Discussion and summary

This study showed the feasibility of OCT microangiography for imaging the microcirculation perfused within ~2 mm in depth from the tissue surface of human cavity *in vivo*. The VCSEL swept-source OCT system provided high-speed imaging (100 FPS for B-scan) with a constant signal sensitivity (105 dB) over the depth range of 4 mm in the experiment, which allowed for fast and high-sensitive 3D OCT imaging of the human cavity tissues. Two types of disposable and detachable small probe attachments were devised and applied to the single OCT probe platform for achieving side and forward view imaging, providing selective and direct access for the probing light to the specific tissue regions inside the cavity. In addition to the ability of identifying the microanatomy (e.g., epithelium, lamina propria and glandular elements) of various mucosal tissues in the oral and the nasal cavity within the penetration depth of 2 mm, the system was also able to delineate characteristic microvasculatures within these tissue regions in three dimensions. Application of the developed novel vessel extraction method in the 3D OCT images enabled to obtain very good quality blood perfusion images, offering visualization of clean vascular morphology.

As mentioned, only a few OCT studies have been dealt with the monitoring of the functions and morphology of the cavity microcirculation of humans in health and disease *in vivo* [43,44]. However, these prior studies have failed to reconstruct the complex microvasculatures of the human cavities either due to the difficulty faced with the accessibility of the inner cavity with the forward imaging probe or due to the unavailability of the techniques suitable for purely extracting the vasculature. The initial findings in this current study showed a great potential of our instrument for mapping 3D microcirculation of the functional vessels in a variety of human cavity tissues including the labial tissue. Further,

#212012 - $15.00 USD Received 13 May 2014; revised 6 Jul 2014; accepted 9 Jul 2014; published 15 Jul 2014

the results as shown here may envision for this OCT microangiography to be used clinically and help in diagnosis for poorly understood pathophysiology of various forms of the cavity diseases *in vivo*.

Despite successfully imaging the cavity microcirculation, the current probe configuration is bulky and limited in length when imaging, which can sometimes be inadequate to access of narrower or deeper cavity tissue areas. In addition, the inner contour shapes of the cavities are often slightly varied among subjects. These factors may make its direct clinical usage difficult. Further miniaturization of the probe attachment and the probe itself in dimensions should resolve this practical concern, allowing for the evaluation of overall cavity microcirculation applicable to all subjects. Also, it would be necessary to improve lateral resolution down to capillary (<8 μm) in order to resolve well the actual microvessels, warranting reliability for measurands in the quantification of the microvessel networks such as vessel diameter or vessel density. With higher axial resolution, however, the mOMAG measurement may be more sensitive to pulsatile bulk motion in axial direction due to its improved resolving ability, resulting in degradation in flow contrast of the angiogram. Lastly, the current swept-source OCT system used in this study still needs some effort to improve its usability to a point that can be operated in at least laboratory environment.

In summary, we have demonstrated the first study of the *in vivo* 3D microcirculation imaging of the wide-range cavity tissues using the single forward/side-viewing probe based VCSEL SS-OCT instrument.

Acknowledgments

This work was supported in part by research grants from the National Institutes of Health (Grant Nos. R01HL093140, R01EB009682, and R01DC010201). The content is solely the responsibility of the authors and does not necessarily represent the official views of grant-giving bodies.